Chapter 4

Experiments with a conducting barrier and a flat base.

This chapter describes the results of a series of measurements taken with an annulus system fully blocked by a thermally conducting barrier and with a flat base, so that the convection chamber had constant depth.

In section 3.4 the prediction was made, according to equations (3.14) and (3.16), that if $\Delta T_B = 0$, then the η-circulation would not occur so that $H_\eta(\bar{r}, a = 0; t) \approx 0$. In an attempt to test this hypothesis, this chapter repeats the experiments of chapter 3 with a thermally conducting barrier, made from a thin sheet of copper. Heat conduction through the barrier might be expected to reduce or at least modify ΔT_B, possibly even to the extent that $\Delta T_B \sim 0$.

4.1 Experimental results.

4.1.1 Velocity measurements.

A regime diagram showing the values of τ and Θ for all the velocity measurements taken with the fully blocking thermally conducting barrier and flat base is shown in *Figure 4.1*. It can be seen that eddies occur for $\Theta \lesssim 0.4$ and for $\tau \gtrsim 9 \times 10^6$, these values are very similar to those seen when an insulating barrier was used (§3.1.1 and *Figure 3.1*).

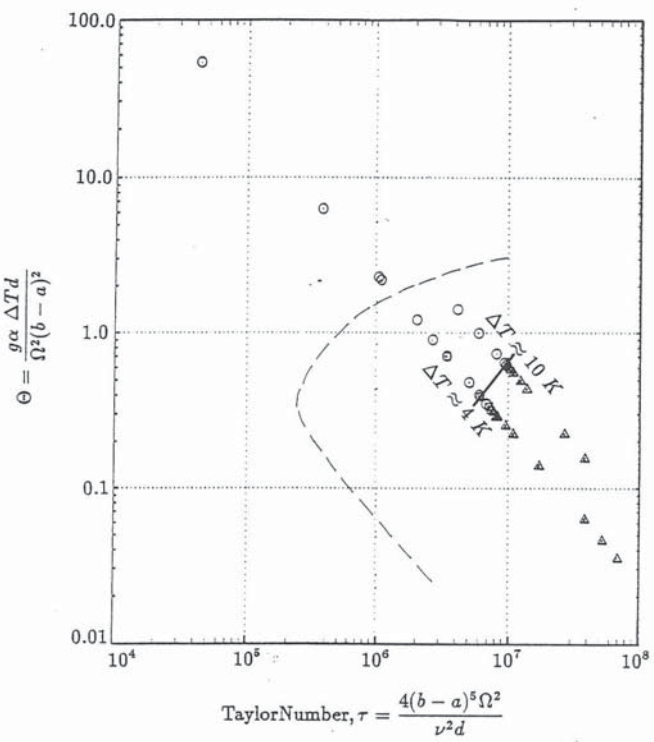

FIGURE 4.1: Regime diagram showing the values of τ and Θ for velocity runs 313-325, E1-E6 and C366-C398, the experiments with the conducting barrier and constant depth, $d = 140\ mm$. The circles show experiments where there were no eddies in the system and the triangles show measurements where eddies were present. The squares show experiments where it was hard to say whether eddies were present or not. The dashed line indicates the approximate location of the transition for the onset of baroclinic waves in an unblocked annulus, such as that used by *W.W.Fowlis and R.Hide (1965)*. The location of the dashed line was obtained from D.W.Johnson (private communication), while the solid line indicates the transition for the onset of eddies in the present experiments.

Figures 4.2 - 4.4 show measurements of horizontal velocities as a regular grid of vectors in an (r, ϕ)-plane. For *Figure 4.2*, $\Omega = 0.49\ rad.sec^{-1}$ and $\Delta T = 4.05\ K$. At the top (a) and bottom (e) of the annulus, radial inflow and outflow can be seen, while prograde flow can be seen by the outer cylinder in (d) and (e). Retrograde flow appears by the inner cylinder in (b), (c), (d) and (e).

Figure 4.3 shows the fluid motions at $\Omega = 1.08\ rad.sec^{-1}$ and $\Delta T = 4.06\ K$. The increase in Ω seems to have resulted in stronger prograde and retrograde flow by the outer and inner cylinders, which can be seen in (b), (c) and (d). The data in (e) is of rather poor quality, as measurements at the bottom of the annulus were sometimes obscured by the beads in the fluid above. However, so far as it is possible to tell, there appears to be radial inflow at the top (a) of the annulus and radial outflow at the bottom (e).

Figure 4.4 shows results for $\Omega = 3.43\ rad.sec^{-1}$ and $\Delta T = 3.99\ K$. The flow has at least one eddy in it, and radial inflow can be seen at the top (a), though the data in (e) is very poor. Prograde flow can be seen by the outer cylinder in (a) - (d), and retrograde flow by the inner cylinder in (c), (d) and possibly (b). Comparison of *Figures 4.2 - 4.4* with *Figures 3.2 - 3.4* shows that there are considerable similarities with the results of the insulating barrier experiments described in chapter 3.

The azimuthal means of the radial components of the fluid velocities shown in *Figures 4.2 - 4.4* are shown in *Figure 4.5*, which shows contours of the radial velocity, u in an (r, z)-plane. *Figure 4.5* clearly shows the radial inflow at the top of the annulus and radial outflow at the bottom. In (a) and (b) the maximum magnitudes of u are fairly similar, but somewhat less in (c), this is not significantly different from the results of *Figure 3.5* as for that case $\Delta T \approx 10\ K$, while in *Figure 4.5*, $\Delta T \approx 4\ K$.

The mean over azimuth of the azimuthal component of velocity is shown in

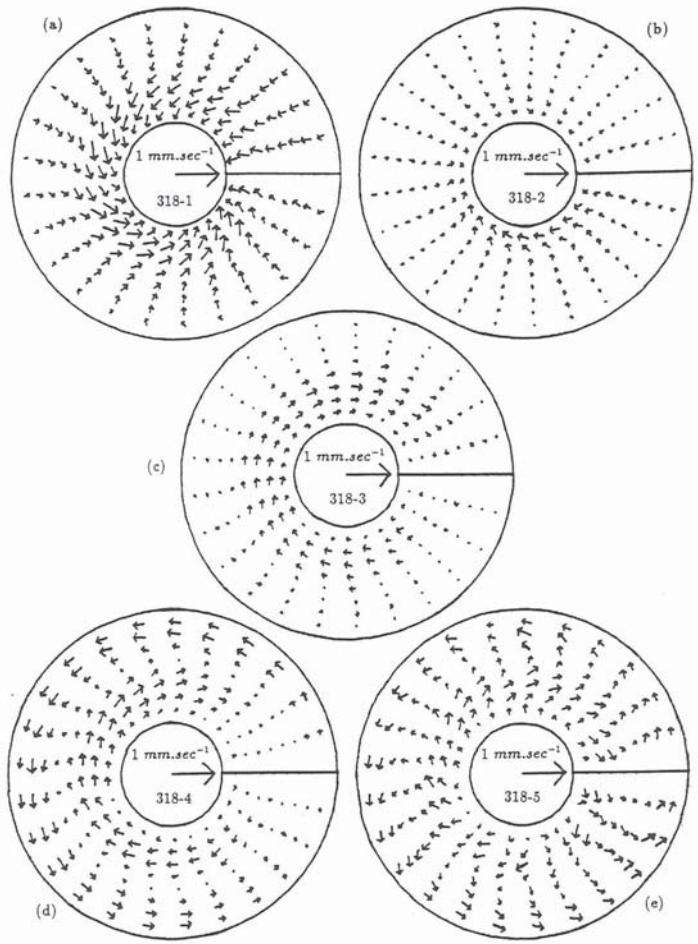

FIGURE 4.2: Horizontal velocity field data from VVAS reprojected onto a regular grid, for the annulus with a full thermally conducting barrier. The location of the barrier is indicated by the solid line in the 3 o'clock position. The flow is shown at various heights above the base of the annulus, these are; (a) 124mm, (b) 97mm, (c) 70mm, (d) 43mm, and (e) 16mm. Data from Run 318, $\Omega = 0.49\ rad.sec^{-1}$, $\Delta T = 4.05\ K$. In each case the central arrow depicts a velocity of 1 $mm.sec^{-1}$. The depth of the annulus was $d = 140\ mm$.

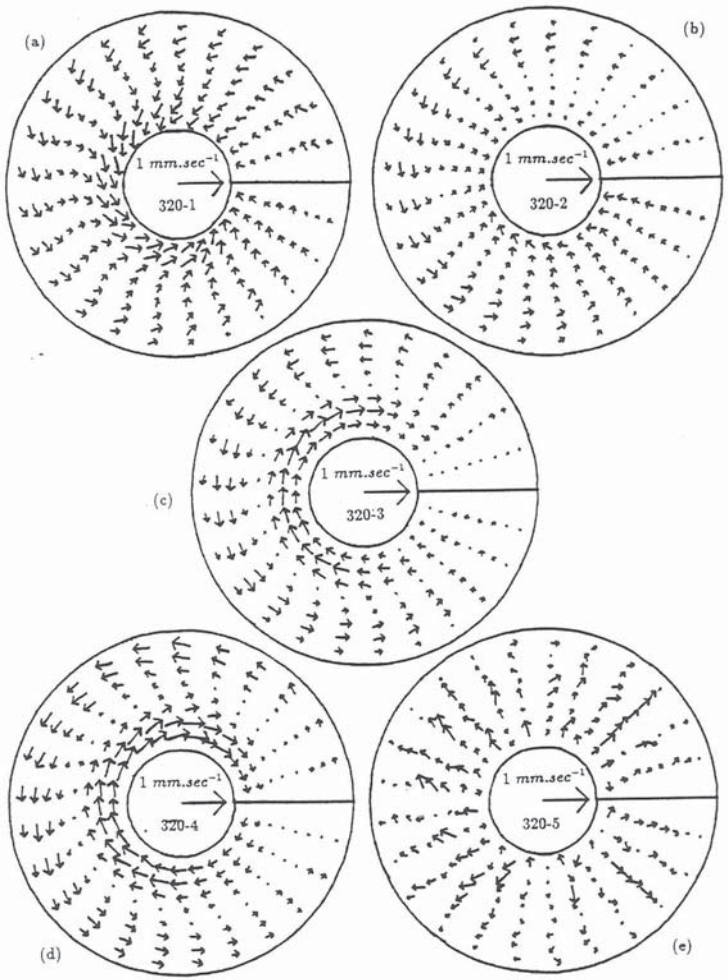

FIGURE 4.3: Horizontal velocity field data from VVAS reprojected onto a regular grid, for the annulus with a full thermally conducting barrier. The location of the barrier is indicated by the solid line in the 3 o'clock position. The flow is shown at various heights above the base of the annulus, these are; (a) 124mm, (b) 97mm, (c) 70mm, (d) 43mm, and (e) 16mm. Data from Run 320, $\Omega = 1.08\ rad.sec^{-1}$, $\Delta T = 4.06\ K$. In each case the central arrow depicts a velocity of 1 $mm.sec^{-1}$. The depth of the annulus was $d = 140\ mm$.

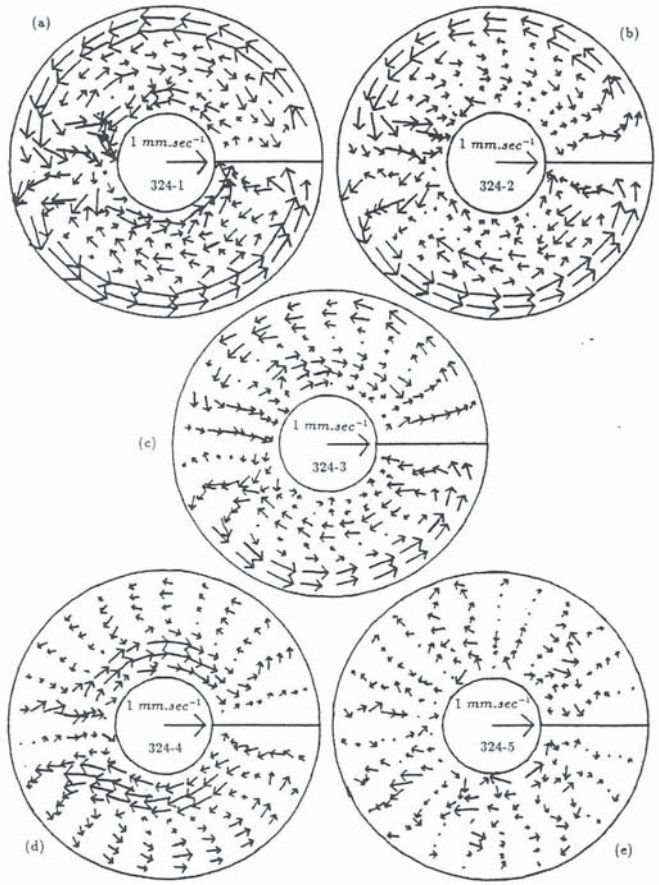

FIGURE 4.4: Horizontal velocity field data from VVAS reprojected onto a regular grid, for the annulus with a full thermally conducting barrier. The location of the barrier is indicated by the solid line in the 3 o'clock position. The flow is shown at various heights above the base of the annulus, these are; (a) 124mm, (b) 97mm, (c) 70mm, (d) 43mm, and (e) 16mm. Data from Run 324, $\Omega = 3.43\ rad.sec^{-1}$, $\Delta T = 3.99\ K$. In each case the central arrow depicts a velocity of 1 $mm.sec^{-1}$. The depth of the annulus was $d = 140\ mm$.

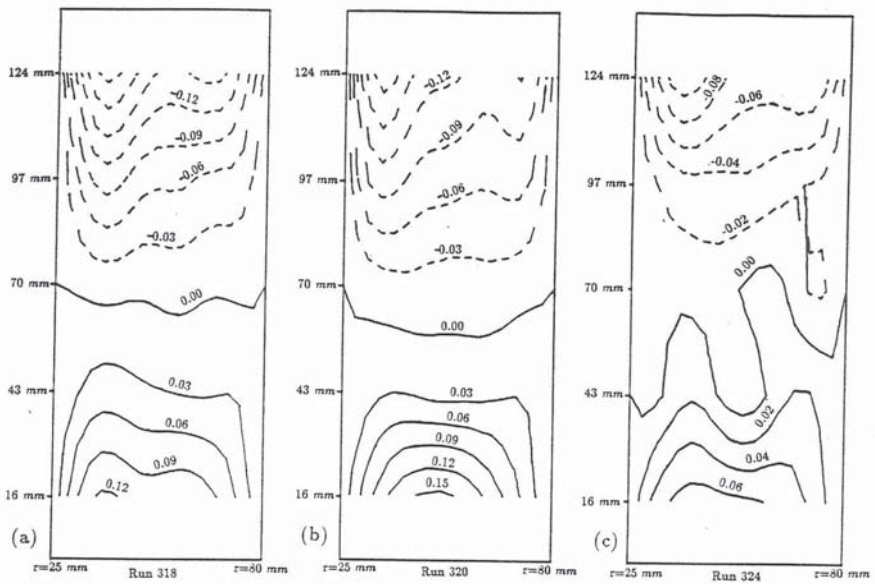

FIGURE 4.5: The figures show contours of the radial component of velocity in $mm.sec^{-1}$ over an (r,z) plane for the annulus with a full insulating barrier and depth, $d = 140\ mm$. Solid contours represent radially outwards flow and dashed contours, inwards flow. (a) Run 318, $\Delta T = 4.05\ K$, $\Omega = 0.490\ rad.sec^{-1}$, (b) Run 320, $\Delta T = 4.06\ K$, $\Omega = 1.080\ rad.sec^{-1}$, and (c) Run 324, $\Delta T = 3.99\ K$, $\Omega = 3.434\ rad.sec^{-1}$. In all cases a clear shear of u with z can be seen, which is suggestive of radial overturning.

Figure 4.6, where contours of v in an (r, z)-plane can be seen. (a) - (c) are the same results used as in *Figures 4.2 - 4.5*. Generally v tends to increase at larger values of Ω. Comparison with *Figure 3.6* shows the results to be rather similar to those obtained with an insulating barrier.

Figure 4.7 shows contours of u in a (ϕ, z)-plane at mid-radius, once again (a) - (c) are the results of *Figures 4.2 - 4.4*. In (a) and (b) the shear of u with both ϕ and z can be seen. In (c) while there are areas where the shear of u with z

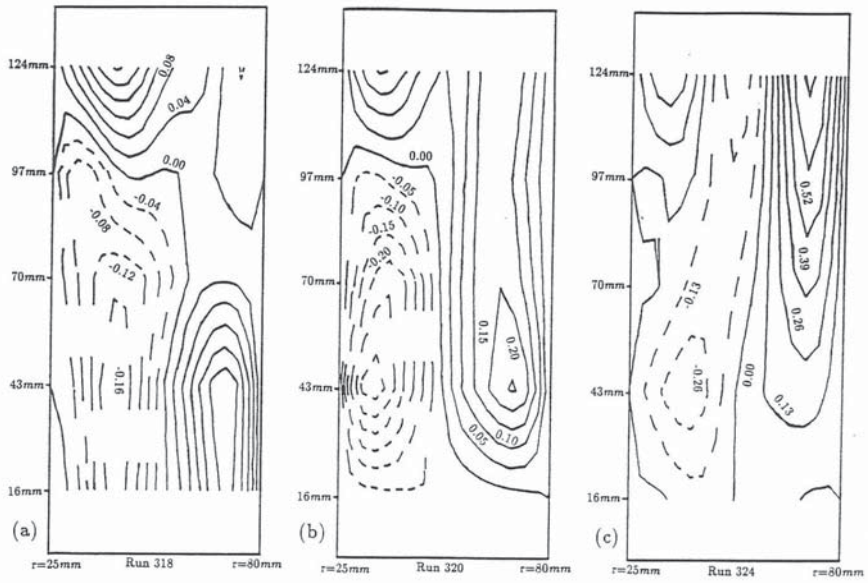

FIGURE 4.6: The figures show contours of the mean over azimuth of v, in $mm.sec^{-1}$ in an (r,z) plane for the annulus with a full insulating barrier and depth, $d = 140\ mm$. Solid contours represent prograde flow and dashed contours, retrograde flow. (a) Run 318, $\Delta T = 4.05\ K$, $\Omega = 0.490\ rad.sec^{-1}$, (b) Run 320, $\Delta T = 4.06\ K$, $\Omega = 1.080\ rad.sec^{-1}$, and (c) Run 324, $\Delta T = 3.99\ K$, $\Omega = 3.434\ rad.sec^{-1}$. The flow patterns appear to be quite complex, with both radial and vertical shear. At mid-height ($z = 0$) the shear of v with r appears to increase with rotation rate.

can be seen, there is a region where u has strong dependence on ϕ, which would appear to correspond to a localized eddy, with relatively little vertical structure. Once again the results of *Figure 4.7* are very similar to those of *Figure 3.7*.

The velocity results are summarized in *Table 4.1*, which in addition to various control parameters and non-dimensional numbers indicates whether eddies were present or not during a measurement under the heading of 'flow type'.

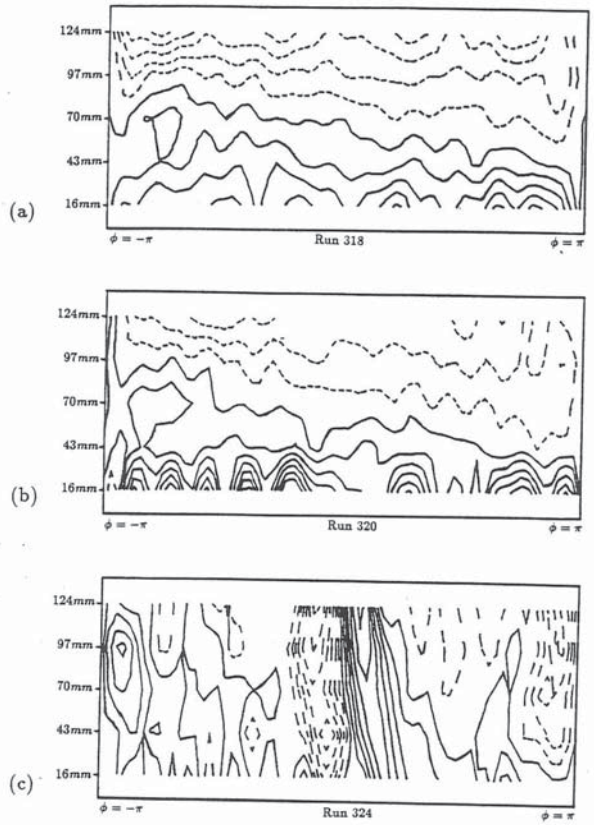

FIGURE 4.7: The figures show contours of the radial component of velocity in an (ϕ, z) plane for the annulus with a full insulating barrier and depth, $d = 140\ mm$. Solid contours represent radially outwards flow and dashed contours, inwards flow. (a) Run 318, $\Delta T = 4.05\ K$, $\Omega = 0.490\ rad.sec^{-1}$, contour interval, $0.04\ mm.sec^{-1}$, (b) Run 320, $\Delta T = 4.06\ K$, $\Omega = 1.080\ rad.sec^{-1}$, contour interval, $0.05\ mm.sec^{-1}$ and (c) Run 324, $\Delta T = 3.99\ K$, $\Omega = 3.434\ rad.sec^{-1}$, contour interval $0.10\ mm.sec^{-1}$. In all cases there is at least a region where a clear shear of radial velocity with height can be seen, which is suggestive of radial overturning. In (a) and (b) there is some indication of a shear of radial velocity with azimuth, while in (c) there is a region of extremely strong azimuthal shear of radial velocity, which must be associated with the eddies seen at this rotation rate.

Run Nº	ΔT K	Ω $rad.sec^{-1}$	Prandtl Nº	Θ	Taylor Nº	Rayleigh Nº	Ekman Nº	Flow type
313	3.89	0.099	14.2	5.36×10^{1}	4.33×10^{4}	8.28×10^{6}	2.96×10^{-3}	no eddies
314	3.94	0.295	14.2	6.15	3.96×10^{5}	8.39×10^{6}	9.96×10^{-4}	no eddies
315	3.94	0.491	14.2	2.21	1.10×10^{6}	8.39×10^{6}	5.97×10^{-4}	no eddies
316	4.14	0.683	14.2	1.21	2.02×10^{6}	8.79×10^{6}	4.34×10^{-4}	no eddies
317	4.05	0.296	14.2	6.32	3.77×10^{5}	8.60×10^{6}	1.00×10^{-3}	no eddies
318	4.05	0.490	14.2	2.30	1.04×10^{6}	8.60×10^{6}	6.05×10^{-4}	no eddies
319	4.02	0.884	14.2	7.01×10^{-1}	3.37×10^{6}	8.54×10^{6}	3.36×10^{-4}	no eddies
320	4.06	1.080	14.2	4.75×10^{-1}	5.03×10^{6}	8.62×10^{6}	2.75×10^{-4}	no eddies
321	4.10	1.275	14.2	3.44×10^{-1}	7.02×10^{6}	8.71×10^{6}	2.33×10^{-4}	no eddies
322	4.02	1.961	14.2	1.42×10^{-1}	1.66×10^{7}	8.54×10^{6}	1.51×10^{-4}	eddies
323	4.00	2.944	14.2	6.30×10^{-2}	3.74×10^{7}	8.50×10^{6}	1.01×10^{-4}	eddies
324	3.99	3.434	14.2	4.62×10^{-2}	5.09×10^{7}	8.48×10^{6}	8.64×10^{-5}	eddies
325	4.06	3.925	14.2	3.59×10^{-2}	6.65×10^{7}	8.62×10^{6}	7.56×10^{-5}	eddies
E1	4.06	1.666	14.2	1.99×10^{-1}	1.24×10^{7}	8.62×10^{6}	1.78×10^{-4}	eddies
E2	4.06	1.471	14.2	2.56×10^{-1}	9.66×10^{6}	8.62×10^{6}	2.02×10^{-4}	eddies
E3	4.08	1.570	14.2	2.26×10^{-1}	1.07×10^{7}	8.67×10^{6}	1.89×10^{-4}	eddies
E4	4.00	1.374	14.2	2.89×10^{-1}	8.15×10^{6}	8.50×10^{6}	2.16×10^{-4}	eddies
E5	3.96	1.277	14.2	3.32×10^{-1}	7.04×10^{6}	8.41×10^{6}	2.32×10^{-4}	eddies
E6	3.95	1.178	14.2	3.88×10^{-1}	6.00×10^{6}	8.39×10^{6}	2.52×10^{-4}	unclear
C366	3.92	1.180	14.2	3.86×10^{-1}	5.99×10^{6}	8.33×10^{6}	2.52×10^{-4}	no eddies
C367	4.04	1.187	14.2	3.91×10^{-1}	6.08×10^{6}	8.58×10^{6}	2.50×10^{-4}	no eddies
C368	3.98	1.266	14.2	3.38×10^{-1}	6.94×10^{6}	8.45×10^{6}	2.34×10^{-4}	unclear
C369	4.08	1.473	14.2	2.56×10^{-1}	9.37×10^{6}	8.67×10^{6}	2.01×10^{-4}	eddies
C370	4.07	0.784	14.2	9.03×10^{-1}	2.66×10^{6}	8.65×10^{6}	3.78×10^{-4}	no eddies
C371	4.00	1.372	14.2	2.90×10^{-1}	8.13×10^{6}	8.50×10^{6}	2.16×10^{-4}	eddies
C372	4.00	0.884	14.2	6.99×10^{-1}	3.37×10^{6}	8.50×10^{6}	3.36×10^{-4}	no eddies
C373	3.95	1.960	14.2	1.40×10^{-1}	1.66×10^{7}	8.37×10^{6}	1.53×10^{-4}	eddies
C374	3.98	1.274	14.2	3.35×10^{-1}	7.01×10^{6}	8.45×10^{6}	2.33×10^{-4}	no eddies
C375	3.99	0.883	14.2	6.99×10^{-1}	3.36×10^{6}	8.48×10^{6}	3.36×10^{-4}	no eddies
C376	3.99	1.176	14.2	3.93×10^{-1}	5.98×10^{6}	8.48×10^{6}	2.52×10^{-4}	no eddies
C377	3.91	1.353	14.2	2.91×10^{-1}	7.90×10^{6}	8.31×10^{6}	2.19×10^{-4}	eddies
C378	3.92	1.294	14.2	3.19×10^{-1}	7.23×10^{6}	8.33×10^{6}	2.29×10^{-4}	eddies
C379	3.97	1.313	14.2	3.14×10^{-1}	7.45×10^{6}	8.43×10^{6}	2.26×10^{-4}	eddies
C380	4.01	1.255	14.2	3.48×10^{-1}	6.80×10^{6}	8.52×10^{6}	2.36×10^{-4}	no eddies

TABLE 4.1: Velocity measurements with a full thermally conducting barrier and a flat base.

Run No	ΔT K	Ω $rad.sec^{-1}$	Prandtl No	Θ	Taylor No	Rayleigh No	Ekman No	Flow type
C381	9.98	1.766	14.2	4.37×10^{-1}	1.35×10^{7}	2.12×10^{7}	1.68×10^{-4}	eddies
C382	10.08	0.980	14.2	1.43	4.14×10^{6}	2.14×10^{7}	3.03×10^{-4}	no eddies
C383	10.04	1.565	14.2	5.59×10^{-1}	1.06×10^{7}	2.13×10^{7}	1.90×10^{-4}	eddies
C384	10.05	1.175	14.2	9.93×10^{-1}	5.97×10^{6}	2.14×10^{7}	2.52×10^{-4}	no eddies
C385	10.04	1.371	14.2	7.28×10^{-1}	8.12×10^{6}	2.13×10^{7}	2.16×10^{-4}	no eddies
C386	9.97	1.460	14.2	6.38×10^{-1}	9.21×10^{6}	2.12×10^{7}	2.03×10^{-4}	no eddies
C387	9.97	1.541	14.2	5.72×10^{-1}	1.06×10^{7}	2.12×10^{7}	1.93×10^{-4}	eddies
C388	10.02	1.480	14.2	6.21×10^{-1}	9.50×10^{6}	2.13×10^{7}	2.01×10^{-4}	no eddies
C389	10.02	1.526	14.2	5.88×10^{-1}	1.00×10^{7}	2.13×10^{7}	1.95×10^{-4}	eddies
C390	10.04	1.510	14.2	6.00×10^{-1}	9.85×10^{6}	2.13×10^{7}	1.97×10^{-4}	eddies
C391	10.02	1.568	14.2	5.56×10^{-1}	1.06×10^{7}	2.13×10^{7}	1.89×10^{-4}	eddies
C392	10.02	1.961	14.2	3.56×10^{-1}	1.72×10^{7}	2.13×10^{7}	1.51×10^{-4}	eddies
C393	9.96	2.450	14.2	2.26×10^{-1}	2.59×10^{7}	2.12×10^{7}	1.21×10^{-4}	eddies
C394	9.97	2.944	14.2	1.57×10^{-1}	3.74×10^{7}	2.12×10^{7}	1.01×10^{-4}	eddies
C395	10.01	1.572	14.2	5.52×10^{-1}	1.07×10^{7}	2.13×10^{7}	1.89×10^{-4}	eddies
C396	9.96	1.675	14.2	4.84×10^{-1}	1.21×10^{7}	2.12×10^{7}	1.77×10^{-4}	eddies
C397	9.97	1.667	14.2	4.89×10^{-1}	1.20×10^{7}	2.12×10^{7}	1.78×10^{-4}	eddies
C398	9.98	1.569	14.2	5.53×10^{-1}	1.06×10^{7}	2.12×10^{7}	1.89×10^{-4}	eddies

TABLE 4.1 (cont.)

4.1.2 Heat and temperature measurements.

A regime diagram showing the values of Θ and τ for all the temperature and heat transport measurements is shown in *Figure 4.8.* Comparison with *Figure 4.1* shows that the eddies formed at slightly larger values of τ (about 2.0×10^7 compared with 0.9×10^7) and slightly smaller values of Θ (around 0.2 instead of 0.4). This corresponds to eddies setting in at a slightly higher value of Ω. This is attributed to the stabilizing effect of the thermocouple ring used in the temperature measurements (see *Hignett et al (1985)*), and the observational difficulties of determining precisely when eddies were present near the transition. However the transition for the onset of eddies still appears to be quite close to that observed when an insulating barrier was used.

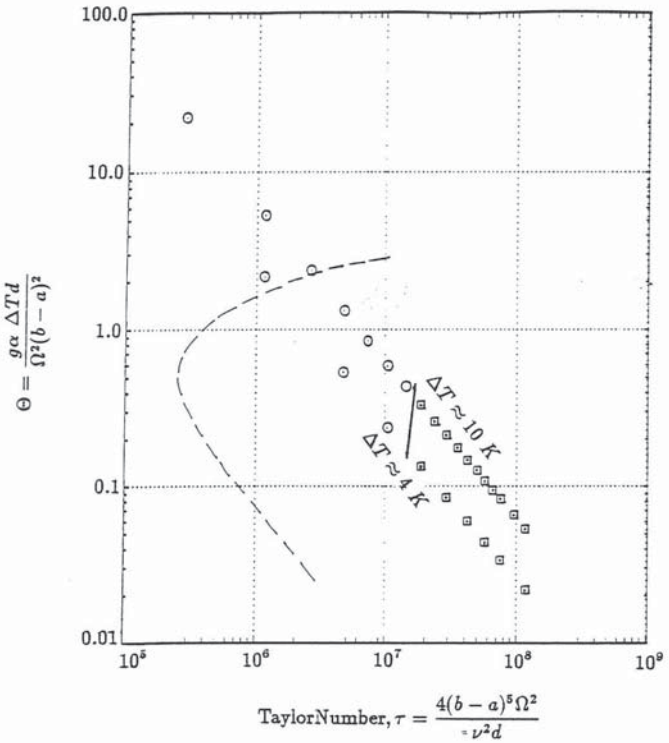

FIGURE 4.8: Regime diagram showing the values of τ and Θ for Runs 012-046, the measurements with the thermally conducting barrier and $d = 140\ mm$. The circles show results where temperature measurements indicated there were no eddies in the system, and the squares show when eddies were present. The dashed line shows the approximate location of the transition for the onset of baroclinic waves in an unblocked annulus, such as that used by *Fowlis and Hide (1965).* The location of the dashed line was obtained from D.W.Johnson (private communication), while the solid line indicates the transition for the onset of eddies in the present experiments.

Figure 4.9 shows the fluid temperature measured by the thermocouple ring at mid-height ($z = 0$) and mid-radius ($r = \bar{r}$); $T(\bar{r}, z = 0; \phi, t)$. Compared with *Figure 3.9* the barrier is shown placed at the centre of the diagram, so that ΔT_B can be seen more clearly. The results are very similar to those of *Figure 3.9*, and the thermally conducting barrier has in no way inhibited the formation of a temperature drop across the barrier. *Figure 4.9 (a)* shows the 'kinks' seen at higher rotation rates, while otherwise the temperature data is very nearly linear.

The increase in ΔT_B with Ω can be seen in *Figure 4.10*. ΔT_B increases linearly with Ω in the same way as the insulating barrier experiments, but levels off at a slightly larger value of ΔT_B ($\sim$ 30% of ΔT) than when the barrier was an insulator.

Figure 4.11 shows plots of Nusselt number against Ω. Comparison with *Figure 3.11* shows that they are remarkably similar. To the accuracy of the error bars the change from an insulating barrier to a conducting barrier has made no difference at all to the Nusselt number.

Table 4.2 summarizes the temperature and heat transport results.

4.1.3 Summary of results.

The observed flow for an annulus with a fully blocking thermally conducting barrier appears to consist of the three main components seen with an insulating barrier (see §3.1), namely (1) a radial overturning, (2) a horizontal circulation with some vertical structure, and (3) eddies which appear at values of $\Theta \lesssim 0.4$ and $\tau \gtrsim 9 \times 10^6$.

Despite the barrier being a thermal conductor, a temperature drop, ΔT_B was observed across it. ΔT_B increased linearly with Ω until a maximum was reached at a value of $\Delta T_B \sim 30\% \Delta T$. This maximum was reached at a value of $\Theta \sim 6.0 \times 10^{-2}$ or 6.6×10^{-2}.

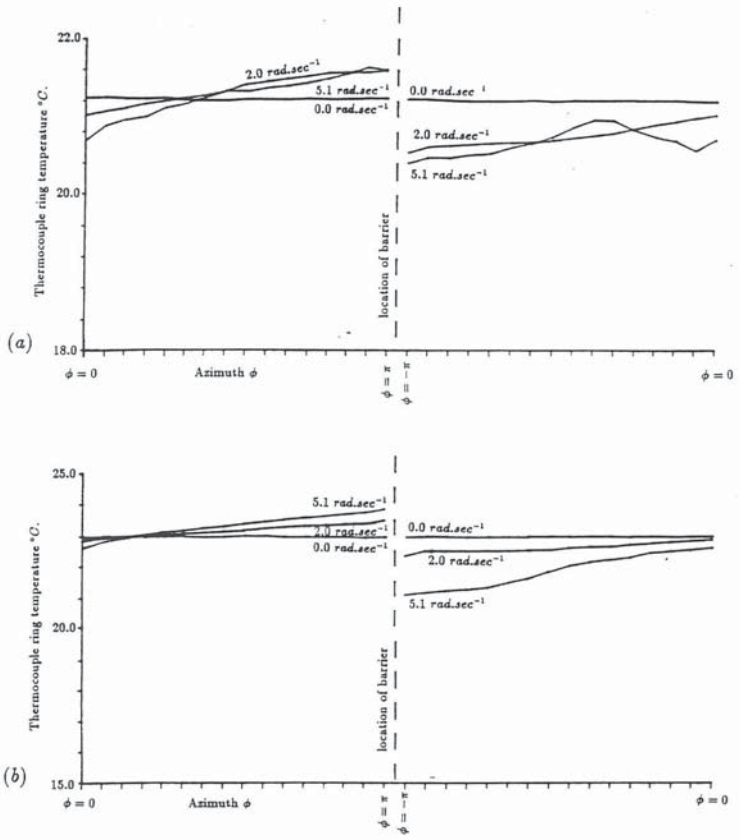

FIGURE 4.9: Experimental results showing temperature of ring thermocouple against azimuthal position for three rotation rates, $\Omega = 0.0, 2.0$ and $5.1\ rad.sec^{-1}$, for the system with constant depth, $d = 140\ mm$ and the thermally conducting barrier. Each of the scale markings along the horizontal axis shows the location of one of the thermocouples in the ring. Measurements of temperature were taken for each thermocouple in the ring, with a straight line drawn between them as a guide to the eye. The standard errors were (a) $0.011°C$, and (b) $0.012°C$. The externally applied temperature differences were (a) $\Delta T \approx 4\ K$, (b) $\Delta T \approx 10\ K$. $\Delta T_B(\Omega)$ was defined as the difference between the maximum and minimum thermocouple ring temperatures for a given Ω. As the figures show ΔT_B was generally the temperature difference between one side of the barrier and the other.

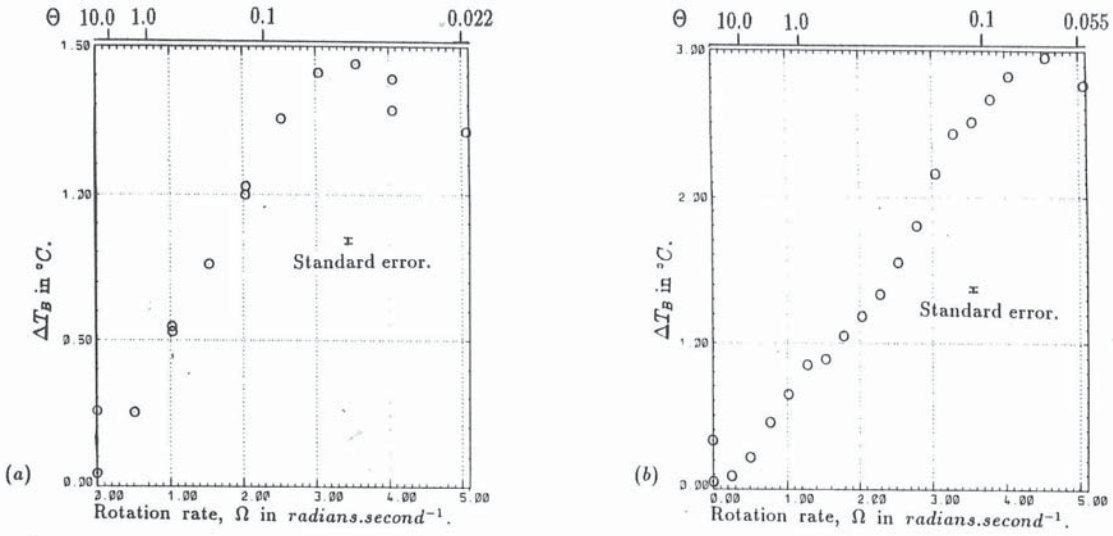

FIGURE 4.10: Experimental results showing dependence of ΔT_B on Ω, for the system with a thermally conducting barrier and depth, $d = 140\ mm$. The externally applied temperature differences were (a) $\Delta T \approx 4\ K$ and (b) $\Delta T \approx 10\ K$.

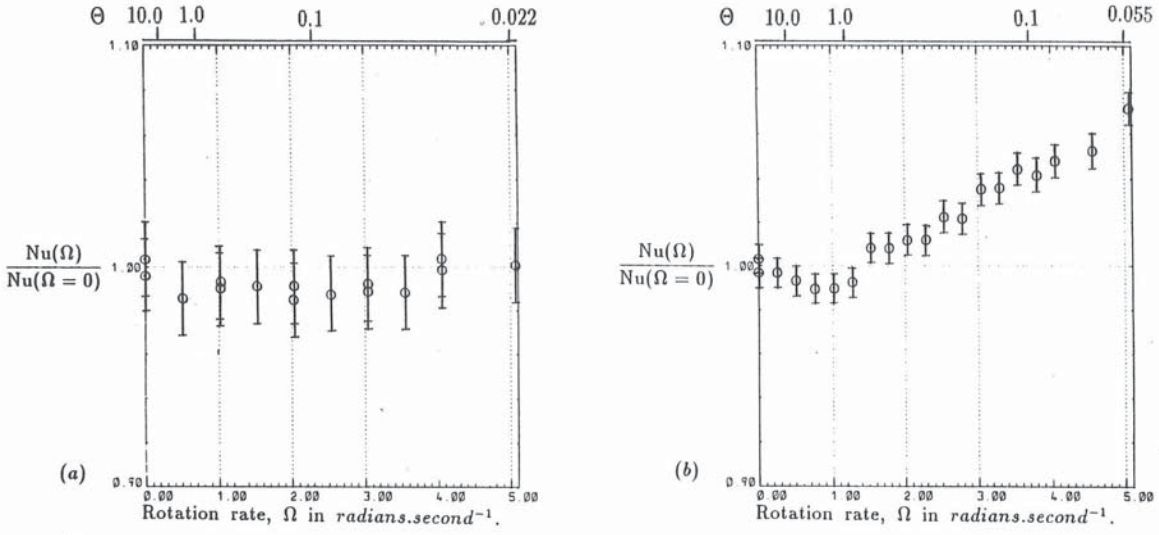

FIGURE 4.11: Experimental results showing the dependence of $Nu(\Omega)/Nu(\Omega = 0)$ on Ω, for the system with a thermally conducting radial barrier and depth, $d = 140\ mm$. The externally applied temperature differences were (a) $\Delta T \approx 4\ K$ and (b) $\Delta T \approx 10\ K$.

Run No	Number of results	ΔT K	Ω $rad.sec^{-1}$	ΔT_{BAR} K	Prandtl No	Θ	Taylor No	Rayleigh No	Ekman No	$H_{conductive}$ $watts$	H_{total} $watts$	Nusselt No
012	181	4.03	0.000	0.25	13.95	∞	0	8.56×10^6	∞	1.58	17.57	11.10
013	241	4.03	0.506	0.25	13.95	2.15	1.14×10^6	8.56×10^6	5.87×10^{-4}	1.58	17.37	10.98
014	241	4.01	1.016	0.55	13.95	5.30×10^{-1}	4.60×10^6	8.52×10^6	2.92×10^{-4}	1.57	17.36	11.03
015	241	4.01	1.522	0.76	13.95	2.36×10^{-1}	1.03×10^7	8.52×10^6	1.95×10^{-4}	1.58	17.39	11.04
016	333	4.01	2.027	1.03	13.95	1.33×10^{-1}	1.83×10^7	8.53×10^6	1.46×10^{-4}	1.58	17.30	10.97
017	361	4.02	2.534	1.25	13.95	8.55×10^{-2}	2.87×10^7	8.55×10^6	1.17×10^{-4}	1.58	17.38	11.00
018	241	4.03	3.038	1.41	13.95	5.96×10^{-2}	4.12×10^7	8.57×10^6	9.76×10^{-5}	1.58	17.45	11.01
019	241	4.03	3.545	1.44	13.95	4.37×10^{-2}	5.61×10^7	8.56×10^6	8.37×10^{-5}	1.58	17.43	11.01
020	241	4.03	4.051	1.28	13.95	3.35×10^{-2}	7.32×10^7	8.56×10^6	7.32×10^{-5}	1.58	17.59	11.12
021	241	4.05	5.064	1.21	13.95	2.15×10^{-2}	1.14×10^8	8.60×10^6	5.86×10^{-5}	1.59	17.73	11.15
042	181	4.02	0.000	0.04	13.95	∞	0	8.53×10^6	∞	1.58	17.62	11.18
043	241	4.02	1.017	0.53	13.95	5.30×10^{-1}	4.62×10^6	8.53×10^6	2.92×10^{-4}	1.58	17.44	11.06
044	401	4.03	2.028	1.00	13.95	1.34×10^{-1}	1.84×10^7	8.57×10^6	1.46×10^{-4}	1.58	17.49	11.04
045	241	4.02	3.037	1.41	13.95	5.95×10^{-2}	4.12×10^7	8.55×10^6	9.77×10^{-5}	1.58	17.46	11.05
046	241	4.05	4.048	1.39	13.95	3.37×10^{-2}	7.32×10^7	8.59×10^6	7.33×10^{-5}	1.59	17.76	11.18

TABLE 4.2: Temperature and heat transport measurements for the annulus with a fully blocking, thermally conducting barrier.

Run No	Number of results	ΔT K	Ω $rad.sec^{-1}$	ΔT_{BAR} K	Prandtl No	Θ	Taylor No	Rayleigh No	Ekman No	$H_{conductive}$ $watts$	H_{total} $watts$	Nusselt No
022	181	9.99	0.000	0.33	13.95	∞	0	2.12×10^7	∞	3.92	55.45	14.14
023	241	9.99	0.506	0.22	13.95	5.32	1.15×10^6	2.12×10^7	5.86×10^{-4}	3.92	54.94	14.00
024	241	10.00	1.016	0.65	13.95	1.32	4.61×10^6	2.12×10^7	2.92×10^{-4}	3.93	54.78	13.95
025	241	10.00	1.523	0.89	13.95	5.88×10^{-1}	1.03×10^7	2.12×10^7	1.95×10^{-4}	3.92	55.76	14.21
026	290	9.99	2.029	1.19	13.95	3.31×10^{-1}	1.84×10^7	2.12×10^7	1.46×10^{-4}	3.92	55.93	14.26
027	361	9.99	2.534	1.55	13.95	2.12×10^{-1}	2.87×10^7	2.12×10^7	1.17×10^{-4}	3.92	56.55	14.41
028	501	9.98	3.039	2.16	13.95	1.47×10^{-1}	4.12×10^7	2.12×10^7	9.76×10^{-5}	3.92	57.20	14.59
029	241	10.00	3.548	2.51	13.95	1.08×10^{-1}	5.62×10^7	2.12×10^7	8.36×10^{-5}	3.92	57.77	14.72
030	241	9.99	4.050	2.82	13.95	8.30×10^{-2}	7.32×10^7	2.12×10^7	7.32×10^{-5}	3.92	57.90	14.77
031	241	9.99	5.063	2.76	13.95	5.31×10^{-2}	1.14×10^8	2.12×10^7	5.86×10^{-5}	3.92	59.22	15.10
032	181	10.01	0.000	0.05	13.95	∞	0	2.13×10^7	∞	3.93	55.20	14.05
033	241	10.00	0.250	0.09	13.95	2.18×10^1	2.80×10^5	2.12×10^7	1.19×10^{-3}	3.92	55.12	14.05
034	241	10.00	0.759	0.45	13.95	2.37	2.57×10^6	2.12×10^7	3.91×10^{-4}	3.93	54.75	13.95
035	241	10.00	1.269	0.85	13.95	8.47×10^{-1}	7.19×10^6	2.12×10^7	2.34×10^{-4}	3.93	54.94	13.99
036	241	10.01	1.775	1.05	13.95	4.33×10^{-1}	1.41×10^7	2.13×10^7	1.67×10^{-4}	3.93	55.85	14.21
037	287	10.01	2.281	1.34	13.95	2.62×10^{-1}	2.32×10^7	2.13×10^7	1.30×10^{-4}	3.93	56.02	14.26
038	401	10.05	2.786	1.80	13.95	1.77×10^{-1}	3.47×10^7	2.14×10^7	1.06×10^{-4}	3.95	56.85	14.40
039	241	10.03	3.292	2.43	13.95	1.26×10^{-1}	4.84×10^7	2.13×10^7	9.01×10^{-5}	3.94	57.52	14.60
040	241	10.02	3.799	2.66	13.95	9.47×10^{-2}	6.45×10^7	2.13×10^7	7.81×10^{-5}	3.93	57.78	14.68
041	241	10.03	4.556	2.96	13.95	6.59×10^{-2}	9.27×10^7	2.13×10^7	6.51×10^{-5}	3.94	58.40	14.83

TABLE 4.2 (Continued.)

The total heat transported by the fluid remains constant against Ω at the $\Omega = 0$ value to within the accuracy of the error bars at $\Delta T \approx 4\ K$. The total heat transport as expressed by the Nusselt number was identical to that observed with an insulating barrier, to within the accuracy of the error bars.

4.2 Discussion of results.

The results with a conducting barrier were very similar to those with an insulating barrier, including the appearance of a temperature drop across the conducting barrier. Thus it was not possible to make $\Delta T_B = 0$ by using a conducting barrier. This in no way disproves the prediction of §3.4 that if $\Delta T_B = 0$ then there should be no η-circulation and that $H_\eta(\bar{r}, a = 0; t) \approx 0$.

While the experiments with the conducting barrier cannot be used to test the prediction of §3.4, they still represent another system which can be used to test the mechanism for the η-circulation in much the same way as the results of chapter 3. The η-circulation and other aspects of the flow are discussed in the following sections, while the remainder of this section considers the remarkable result of the appearance of quite a large temperature drop (ΔT_B) across the conducting barrier.

The thermocouple ring measurements in *Figure 4.9* show virtually no sign of a convergence of fluid temperatures towards the sides of the conducting barrier. The largest values of ΔT_B were about $0.3\Delta T$. If this temperature difference were to be applied (azimuthally) directly across the copper barrier, then using $k_{copper} = 401\ watts.m^{-1}.K^{-1}$, a barrier thickness of 0.49mm, and an area of $(b-a)d$, the heat conduction through the barrier would be $1890\Delta T\ watts$. Using the insulating barrier results of chapter 3, a temperature difference of $0.25\Delta T$, applied across a sheet of perspex ($k_{plastic} \approx 0.2\ W.m^{-1}.K^{-1}$) of thickness 2.5mm, gives a heat conduction through the barrier of $0.154\Delta T\ watts$. Expressed in

this way the values of ΔT_B seen across the thermally conducting barrier seem quite remarkable. Since such a large heat conduction would completely dwarf the total heat transport by the fluid, it seems likely that some sort of boundary layer must form to each side of the barrier. However the thermal structure of this proposed boundary layer must be thin enough so that it is not measured by the thermocouples closest to the sides of the barrier, which are about 5mm away from it. Since the barrier appears to be a hot vertical surface to fluid on the cold side of the barrier (and vice–versa for fluid on the hot side) it seems reasonable to suppose that if a boundary layer were to form it might be rather like one of the side wall (at $r = a, b$) boundary layers. The computor model results of chapter 5 (*Figure 5.6 (c)*) suggest that a side wall boundary layer might be characterised by a balance between buoyancy, viscous and pressure gradient forces and have a thickness a little less than 5mm or so.

To explore this idea a little further a simple form of boundary layer is suggested below, and the fluid velocity associated with it estimated from scaling–type arguments.

The simplified boundary layer has the azimuthal heat conduction through it balanced by advection of heat by w, where w arises from a balance between the buoyancy and viscous forces. Thus from equation (1.5)

$$w\frac{\partial T}{\partial z} \approx \frac{\kappa}{r}.\frac{\partial T}{\partial \phi} \quad \Rightarrow \quad \frac{w\Delta T}{d} \sim \frac{\kappa 0.3\Delta T}{2\delta},$$

where δ is the thickness of the boundary layer (i.e. 5mm). Only one–half of ΔT_B has been applied across the boundary layer, as there is assumed to be a similar boundary layer on the other side of the barrier. The above leads to an estimated value for w in the boundary layer of $5.4\ cm.sec^{-1}$. If w arises from a balance between buoyancy and viscous forces, then from equation (1.6)

$$g\alpha(T - \bar{T}) \approx \nu\nabla^2 w \quad \Rightarrow \quad \frac{g\alpha 0.3\Delta T}{2} \sim \frac{\nu w}{\delta^2},$$

where one–half of ΔT_B has again been applied across the boundary layer, and δ is assumed to be so much smaller than the other length scales implicit in the operator ∇^2 that they may be neglected. The above leads to an estimate for w of $0.6\Delta T$ $cm.sec^{-1}$, i.e. between 2.5 and 6.0 $cm.sec^{-1}$. Thus though the values for w do appear to be quite large, the w estimated from consideration of the balance of forces in the proposed boundary layer would probably be sufficient to advect enough heat to prevent a rise in fluid temperature immediately outside the boundary layer.

The above suggests that it is quite possible that some interesting boundary layer structure exists to the sides of the conducting barrier, which may be worth further investigation.

4.2.1 The η-circulation.

Changing the thermally insulating barrier to a conductor means that the measurements of total heat transport include a contribution due to thermal conduction through the barrier from $r = b$ to $r = a$. This was reduced by insulating the barrier from the sides of the chamber using plastic edging 0.94 mm thick. The radial heat conduction through the conducting barrier was estimated at ~ 0.07 *watts* in chapter 2, the standard errors in the total heat transport were 0.22 *watts* so radial heat conduction through the barrier may be neglected.

As the results of the experiments with the conducting barrier were so similar to those with an insulating barrier, the simplified interpretation of the flow pattern is valid for these results also (§3.2.1 and *Figure 3.12*).

The dimensions of the convection chamber remained unchanged, so the theory relating to heat advection in §3.2 applies equally to the conducting barrier measurements. Thus it is to be expected that equations (3.14) and (3.16) describe the η-circulation with a conducting barrier, and that a plot of A_*^{-1} against Ω

(equation (3.17)) should give results very similar to those of *Figure 3.13*. *Figure 4.12* shows plots of A_*^{-1} against Ω for the two values of ΔT used in the conducting barrier experiments. It can be seen that $A_*^{-1} \approx 0.78$, giving $A_* \approx 1.27$, for $\Omega \lesssim 3.0$ $rad.sec^{-1}$ and $\Delta T = 4$ K. A similar value is seen for $\Delta T = 10$ K, but over a larger range of Ω. Comparison with *Figure 3.13* shows that the variation of A_* with Ω is very similar to the insulating barrier experiments, though the value of A_*^{-1} is somewhat smaller (for given Ω) for the conducting barrier experiments than the insulating barrier experiments. Equation (3.17) shows that this can be traced to the fact that the values of ΔT_B were greater for the conducting barrier experiments than the insulating barrier experiments.

Using equation (3.20) it is possible to plot $Y(\bar{r}, a = 0; \Omega, t)$ against ΔT_B, to give *Figure 4.13*, which again shows good agreement with the empirical equation.

The fact that $H_{adv}(\bar{r}; \phi, z, t)$ was very similar for both the insulating and conducting barrier experiments (compare *Figures 3.11* and *4.11* and *Figures 3.17* and *4.16*) suggests that equation (3.16) can be equated for the heat advection of the η-circulation for each of the two cases (insulating and conducting). This predicts that for a given ΔT and Ω, ΔT_B should be the same for both the insulating and conducting barrier experiments, which amounts to saying that A_* should be the same in both cases, using equation (3.17). However if the approximation that $\Delta T_z \approx \Delta T$ is not used in (3.16) a different relation can be derived, namely

$$(\Delta T_B \Delta T_z)_{insulating} \approx (\Delta T_B \Delta T_z)_{conducting}, \tag{4.1}$$

for a given Ω and ΔT. Where the subscripts '*insulating*' and '*conducting*' refer to measurements taken with an insulating or conducting barrier. This equation suggests an explanation as to why the advective heat transports for the two sets of experiments are the same, though $\Delta T_B(\Omega)$ is different. Since ΔT_B for the conducting barrier is greater than ΔT_B for the insulating barrier, it follows from

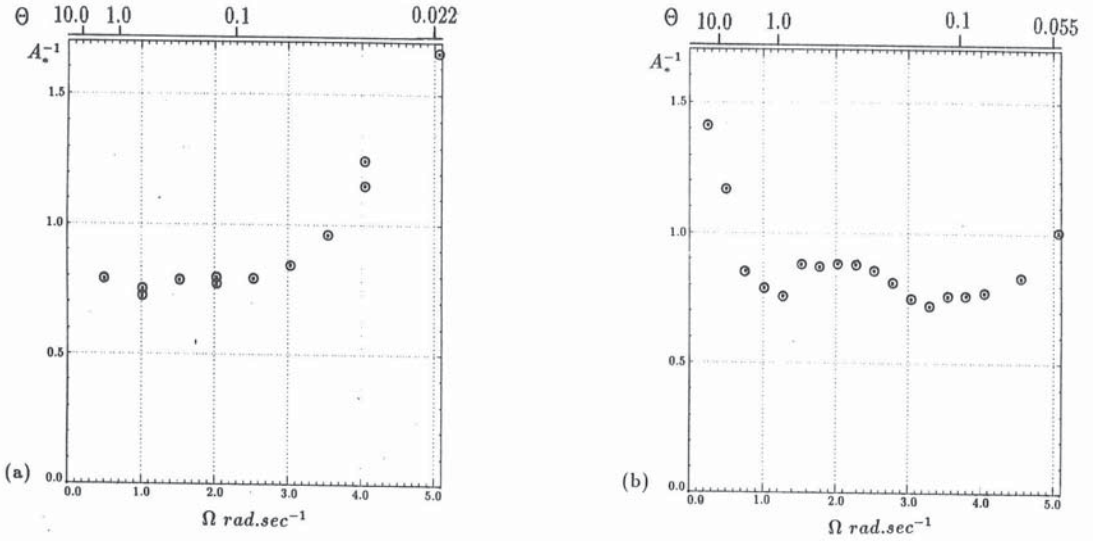

FIGURE 4.12: Plots of the quantity $A_*^{-1} = 24\Omega H(\rho C_P g\alpha\ \Delta T d^2 \Delta T_B)^{-1}$ against Ω for the system with a thermally conducting barrier and $d = 140\ mm$. (a) $\Delta T \approx 4\ K$, (b) $\Delta T \approx 10\ K$. In both cases $A_*^{-1} \sim 1$. For Ω greater than about $3.0\ rad.sec^{-1}$ for (a) A_*^{-1} increases fairly rapidly with rotation rate.

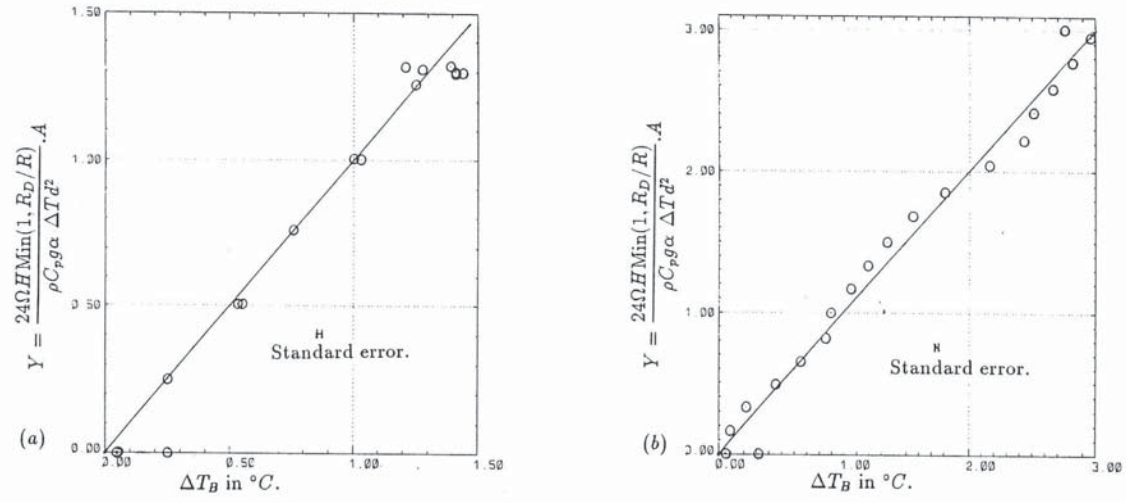

FIGURE 4.13: Plots of the quantity $Y = 24\Omega H \mathrm{Min}(1, R_D/R) A(\rho C_p g\alpha\ \Delta T d^2)^{-1}$ against experimental measurements of ΔT_B for the system of constant depth $d = 140\ mm$, with a thermally conducting barrier. In both cases the results fall quite closely onto a straight line of gradient unity, indicating that $\Delta T_B \approx Y$. For (a) $\Delta T \cong 4\ K$, $A = 1.27$, $R = 0.78\ cm$, and (b) $\Delta T \cong 10\ K$, $A = 1.27$, $R = 0.75\ cm$.

(4.1) that ΔT_z for the conducting barrier must be less than ΔT_z for the insulating barrier. Thus in the case of an insulating barrier (using equation (3.14)) since ΔT_B is smaller, the η-circulation must be weaker. However the larger value of ΔT_z means that it transports just as much heat as the conducting barrier case, where though the η-circulation is stronger (because ΔT_B is larger) its heat advection is no larger because in that case ΔT_z is less.

Equation (4.1) could be tested by a set of experiments where ΔT_B and ΔT_z were measured simultaneously for both insulating and conducting barriers, and plotted as a function of Ω for a given value of ΔT. The velocity data is not suitable to compare the relatively small differences in the magnitude of the η-circulations in each case (through equation (3.14)), due to the errors involved.

Table 4.3 gives the maximum positive and negative values of the azimuthally averaged radial component of velocity, and *Figure 4.14* shows these plotted against Ω, in the same way as *Figure 3.15*. To the accuracy of the error bars u is constant with Ω upto $\Omega \sim 3.0\ rad.sec^{-1}$, which is in agreement with the mechanism proposed for the η-circulation, as expressed in equation (3.14).

$\Delta T \approx 4\ K$						
Run No	Ω $rad.sec^{-1}$	Max $u>0$ $mm.sec^{-1}$	Max $u<0$ $mm.sec^{-1}$	Max $v>0$ $mm.sec^{-1}$	Max $v<0$ $mm.sec^{-1}$	Error in u $mm.sec^{-1}$
313	0.099	0.12	-0.16	0.04	-0.04	0.09
314	0.295	0.11	-0.23	0.17	-0.09	0.09
315	0.491	0.10	-0.22	0.27	-0.21	0.09
316	0.683	0.10	-0.22	0.26	-0.21	0.09
317	0.296	0.13	-0.24	0.18	-0.11	0.09
318	0.490	0.12	-0.22	0.24	-0.19	0.09
319	0.884	0.11	-0.21	0.29	-0.26	0.09
320	1.080	0.16	-0.20	0.26	-0.34	0.09
321	1.275	0.17	-0.20	0.31	-0.35	0.09
322	1.961	0.12	-0.17	0.49	-0.22	0.09
323	2.944	0.10	-0.09	0.73	-0.23	0.09
324	3.434	0.07	-0.11	0.81	-0.36	0.09
325	3.925	0.04	-0.05	0.71	-0.37	0.09

TABLE 4.3: Measurements of the maximum positive, and maximum negative values of the radial and azimuthal components of velocity, for the experiments with a fully blocking, thermally conducting radial barrier.

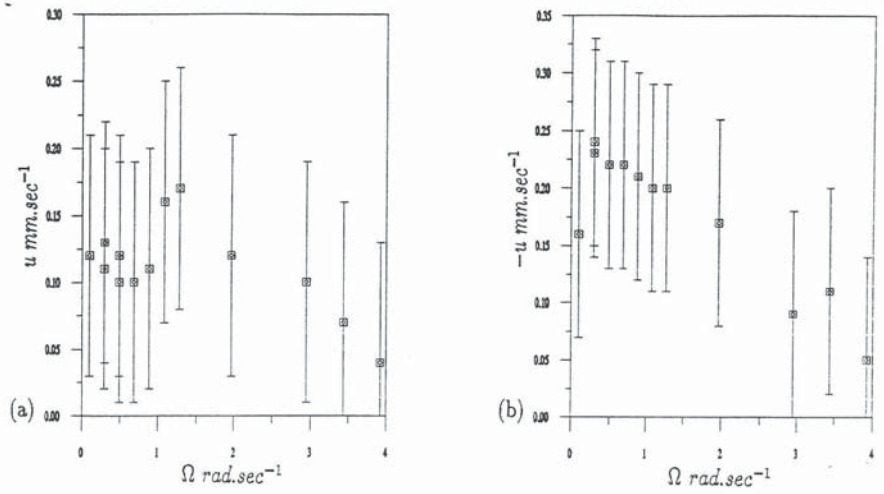

FIGURE 4.14: Plots of (a) maximum positive u, and (b) maximum negative u, against Ω for $\Delta T \approx 4\ K$, using the velocity results given in *Table 4.3*. The measurements show that u remains constant with Ω for $\Omega \lesssim 3.0\ rad.sec^{-1}$, to the accuracy of the error bars. This result is consistent with equation (3.14) and the mechanism for the η-circulation (see §4.2.1).

4.2.2 Heat advection by other processes.

Following the approach of §3.2.5, *Figure 4.15* shows a plot of the maximum positive and negative values of the azimuthal component of velocity, v against Ω, from which it can be seen that

$$|v| \approx 0.02\Omega\ cm.sec^{-1}.$$

As this is the same result as was obtained with the insulating barrier results, $H_\zeta(\bar{r}, a = 0; \phi, t)$ was assumed to be estimated by equation (3.23). The values of $H_\zeta(\bar{r}, a = 0; \phi, t)$ are plotted in *Figure 4.16* along with the heat transport contributions of other effects.

Figure 4.7(c) allows the radial velocity shear with ϕ of the eddy to be

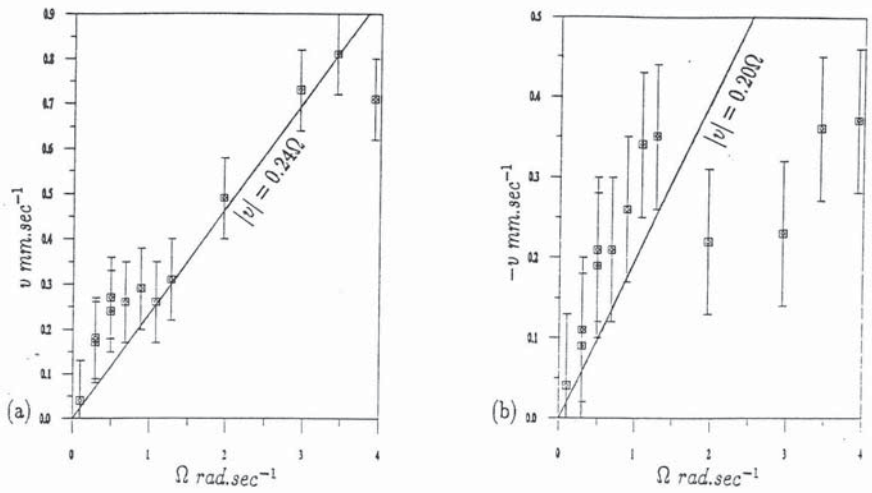

FIGURE 4.15: Plots of (a) maximum positive, and (b) maximum negative, v against Ω for $\Delta T \approx 4\ K$, using the velocity results given in *Table 4.3*. Also plotted are solid lines, showing that $|v| \approx 0.2\Omega\ mm.sec^{-1}$. The four data points at high Ω in (b) were considered to probably be in error, by comparison with (a) and *Figure 3.16 (a)-(d)*.

estimated as $\Delta u_B \sim 0.80\ mm.sec^{-1}$. The appropriate value of $\Delta T'$ was $0.442\ K$, so that the order of magnitude estimate of the maximum heat advection by eddies (see §3.2.6) is

$$H'(\bar{r};\phi,z,t) \sim \bar{\rho}\bar{C}_p \Delta u_B \Delta T' \bar{r} d \frac{2\pi}{5} = 14\ watts.$$

Comparison with *Figure 4.16* shows this to be a little on the large side again, but clearly eddies are quite capable of transporting significant amounts of heat.

The quantity $H_0'(\bar{r}, a = 0; \phi, t)$ given in equation (3.25) was calculated for the measurements and plotted in *Figure 4.16*. Again the values of H_0' are rather small, the same result as found in §3.2.6.

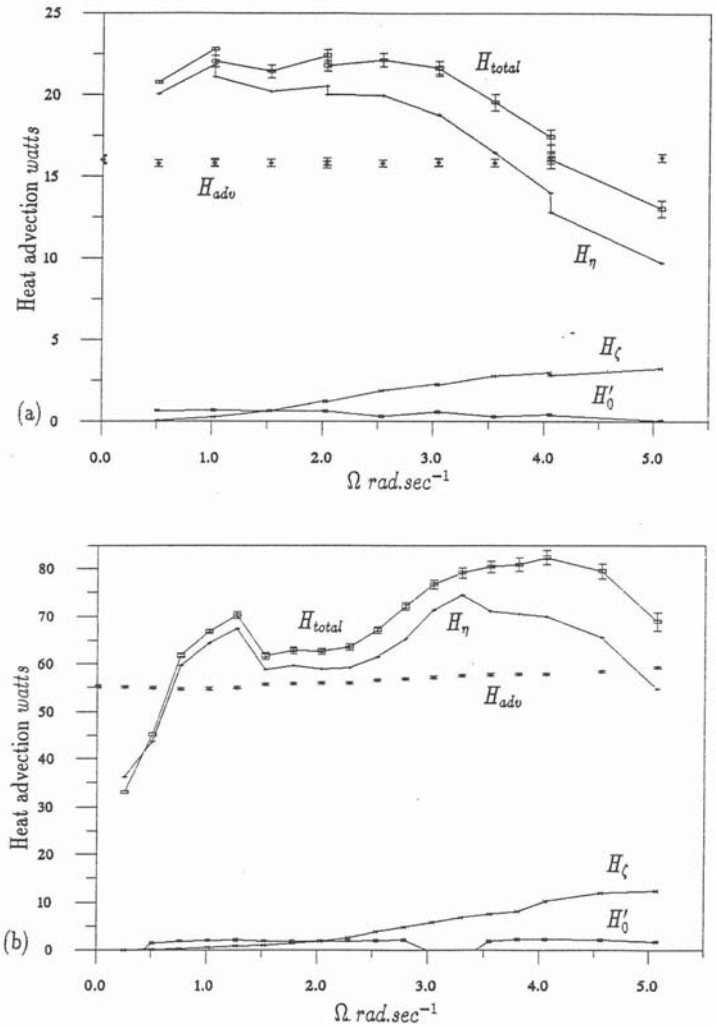

FIGURE 4.16: Plots showing the heat transport contributions for the conducting barrier. Heat transport contributions have been calculated for; the η-circulation, H_η, using equation (3.16); the ζ-circulation, H_ζ, using equation (3.23); and H_0', using equation (3.25). $H_{total} = H_\eta + H_\zeta + H_0'$. Experimental measurements of the advective heat transport, H_{adv} are shown for comparison. (a) $\Delta T \approx 4\ K$, (b) $\Delta T \approx 10\ K$. The lines serve only as a guide to the eye.

4.3 Conclusions.

Section 4.1.3 gives a summary of the experimental results. Using a thermally conducting barrier did not cause ΔT_B to become zero, or even to be reduced. Hence, while the measurements with a conducting barrier did not enable the desired test of the η-circulation to be made, the results (see §4.2.1) were in agreement with the theory for the η-circulation proposed in §3.2.3.

A further result is that changing the barrier from a thermal insulator to a conductor does not greatly affect the total heat transport measurements.

The reasons as to why ΔT_B should be larger for a conducting barrier than an insulating barrier have not been investigated. However equation (4.1) suggests that the heat transport in the two systems is the same because the value of ΔT_B can only be increased at the expense of ΔT_z. This means that while the velocities of the η-circulation with a conducting barrier should be stronger by about the ratio of the two ΔT_B's at a given Ω (see equation (3.14)), the modifications to the temperature field that take place cause the heat advection to remain the same. Equation (4.1) further suggests that ΔT_z is over estimated by ΔT. These suggestions can be tested by the series of experiments mentioned in §4.2.1.

Since $H_\eta(\bar{r}, a = 0; t)$ is given by equation (3.16), the fact that the estimate of $\Delta T_z \approx \Delta T$ is too large would explain why the values of H_η and H_{total} plotted in *Figure 4.16* are somewhat on the large side. If H_η is to equal H_{adv} in *Figure 4.16* then it should be reduced to about 80% of its current value, which by equation (3.16), suggests that for the conducting barrier experiments $\Delta T_z \sim 80\% \Delta T$. This is equivalent to saying that the ratio of ΔT_z to ΔT is the same as the ratio between the value of A_*^{-1} (at low to moderate Ω) and its theoretical value of 1.0.

Bowden's (1961) result (equation (3.26)) may again be applied to the heat transport when $\Omega = 0$, since when the annulus is stationary there is no flow in the ϕ-direction. Thus *Table 4.4* shows equation (3.26) tabulated against $\mathrm{Nu}(\Omega = 0)$,

in the same way as §3.3. It can be seen that there is excellent agreement with equation (3.26).

A possibly unexpected result was that the fluid was able to support a (relatively) large temperature drop across the thermally conducting barrier (ΔT_B). The arguments of §4.2 suggest that a boundary layer with a thickness of $\sim 5mm$ may have formed to each side of the barrier. Further experiments to explore the nature of the flow close to the side of the barrier might be able to establish whether there is a boundary layer by the sides of the barrier, and if so, what its structure is.

Run No	$\Delta T\ ^\circ C$	Nu	$0.203\mathrm{Ra}^{1/4}$	$\pm 0.010\mathrm{Ra}^{1/4}$
012	4.03	11.10	10.98	0.54
042	4.02	11.18	10.97	0.54
022	9.99	14.14	13.78	0.68
032	10.01	14.05	13.79	0.68

TABLE 4.4: Values of Nu at $\Omega = 0$ for the measurements made with a fully blocking thermally conducting barrier, compared with equation (3.26).